PAPER

Non-volatile organic field-effect transistor memory comprising sequestered metal nanoparticles in a diblock copolymer film†

Chia-Min Chen,[a] Chih-Ming Liu,[a] Kung-Hwa Wei,[*a] U-Ser Jeng[b] and Chiu-Hun Su[b]

In this study, we fabricated p-channel-type non-volatile organic field-effect transistor (OFET) memory devices featuring an asymmetric PS-*b*-P4VP diblock copolymer layer incorporating high- and low-work-function metal nanoparticles (NPs) in the hydrophilic and hydrophobic blocks, respectively. We chose the highly asymmetric diblock copolymer PS_{56k}-*b*-$P4VP_{8k}$ as the polymer electret to create the memory windows, and used the different work functions of the *ex situ*-synthesized metal NPs to tune the memory window for either p- or n-channel applications. The transfer curves of non-volatile OFET memory devices incorporating an asymmetric PS_{56k}-*b*-$P4VP_{8k}$ layer embedded with high-work-function Pt NPs (5.65 eV) in the P4VP block exhibited a positive threshold voltage shift and a large memory window (*ca.* 27 V). In contrast, the transfer curves of the corresponding non-volatile OFET memory devices featuring embedded low-work-function (4.26 eV) Ag NPs exhibited a negative threshold voltage shift and a smaller memory window (*ca.* 19 V). This approach provides a versatile way to fabricate p- or possibly n-channel-type non-volatile organic field-effect transistor (OFET) memory devices with the same processing procedure.

Introduction

Organic non-volatile memory (ONVM) is an emerging research field that takes advantage of the properties of organic materials, such as good scalability, mechanical strength, and flexibility, easy processing, and the ability to perform three-dimensional (3D) stacking at low cost. Based on their structures, organic memory cells can be divided into three categories: two-terminal organic bistable devices,[1–4] metal–insulator–semiconductor devices,[5,6] and three-terminal organic field-effect transistors (OFETs) with memory layers.[7–9] OFETs with non-volatile memory are promising candidates for future applications because of their nondestructive reading behavior and direct integrated circuit architectural compatibility. Based on their operating mechanisms, OFET-type memory devices can be further subdivided into four categories: (i) polymeric electret storage,[8,9] where a single organic polymer gate dielectric layer possesses both charge tunneling and trapping abilities; (ii) floating gate storage,[10,11] where charges are injected from the silicon substrate

across the first insulator and stored in the floating gate; (iii) ferroelectric storage,[12,13] in which a memory cell with an OFET structure features an organic material (*e.g.*, hexathiophene) as the active layer and an inorganic ferroelectric material (*e.g.*, PbZr TiO_3) as the gate dielectric layer; and (iv) other types of storage,[14,15] using nanostructured materials [*e.g.*, nanoparticles (NPs) or quantum dots (QDs)] as the memory center. Previous studies on the memory characteristics of ONVM devices have mainly been concerned with altering the chemical structures of the organic materials or the buffer layers. For example, the memory properties of ONVM devices[9] fabricated based on a pentacene OFET with nonpolar polymers [such as polystyrene (PS), poly(α-methylstyrene) (PαMS) and poly(2-vinyl naphthalene) (PVN)] exhibited non-volatile OFET memory characteristics superior to those incorporating polar polymers [such as poly(vinyl alcohol) (PVA), poly(4-vinyl phenol) (PVP) and poly(2-vinyl pyridine) (PVPyr)]. Moreover, bilayers of PS (polymer electret) and Au NPs (negative charge trapping) can be used to control the threshold voltage shift.[11]

Recently, much attention has been focused on the development of block copolymer/metal NP composites for ONVM devices, due to the good electron trapping ability of metal NPs and the ability of nanostructured block polymers to self-assemble with NPs into ordered structures.[16,17] For example, OFET-type memory devices featuring *in situ* prepared[18–21] Au NPs incorporated into the P4VP domains of a poly(styrene-*block*-4-vinyl-pyridine) (PS_{12k}-*b*-$P4VP_{15k}$) diblock copolymer micelle monolayer thin film had a memory window of 9–11 V.[22]

[a]Department of Materials Science and Engineering, National Chiao Tung University, 1001 Ta Hsueh Road, Hsinchu, 30050, Taiwan, ROC. E-mail: khwei@mail.nctu.edu.tw; Fax: +886-3-5724727; Tel: +886-3-5731771

[b]National Synchrotron Radiation Research Center, 101 Hsin-Ann Road, Science-Based Industrial Park, Hsinchu, 30077, Taiwan, ROC

† Electronic supplementary information (ESI) available: TEM images of the DT-Ag and Py-Pt NPs; cross-sectional TEM images of the (DT-$Ag_{0.8}$@PS)-*b*-(Py-$Pt_{1.0}$@P4VP) and neat PS-*b*-P4VP films; EDX spectra of the (DT-$Ag_{1.0}$@PS)-*b*-(Py-$Pt_{1.0}$@P4VP) composite; thermal stability; NP trapping strategy. See DOI: 10.1039/c1jm13936c

Because the nonpolar PS block can provide better memory performance than that of the polar P4VP block, in this present study we probed the memory characteristics of OFETs with *ex situ* synthesized[23–26] metal NPs sequestered in the nonpolar PS-block or in the polar P4VP-block of an asymmetric PS-*b*-P4VP diblock copolymer. We chose the highly asymmetric diblock copolymer PS$_{56k}$-*b*-P4VP$_{8k}$ as the polymer electret to create the memory windows, and used the different work functions of the *ex situ* synthesized metal NPs to tune the memory window for either p- or n-channel applications. We incorporated *ex situ* synthesized dodecanethiol-passivated silver (DT-Ag) and pyridine-coated platinum (Py-Pt) NPs in the PS and P4VP blocks, respectively. The reason we selected *ex situ* synthesized Ag and Pt NPs for this study was the large difference (1.39 eV) between their work functions (4.26 eV for Ag; 5.65 eV for Pt) and because their surface ligands can be tailored to ensure miscibility in the particular polymer domains. We expected the transfer curves of the OFETs featuring the embedded Pt and Ag NPs to exhibit positive and negative threshold voltage shifts, respectively, for applications in p- and n-channel memory transistors, respectively. These applications could be integrated to form the element logic cell of the complementary metal–oxide–semiconductor (CMOS) structure in integrated circuits. The one-step fabrication of arrays of metallic NPs through spin-coating processing makes this approach potentially amenable to the construction of NP-based organic memory devices.

Fig. 1 provides a schematic representation of the steps involved in fabricating the devices. The inset presents the chemical structure of PS-*b*-P4VP. The diblock copolymer and various amounts of metal NPs were dissolved in toluene and then spin-coated on a 200 nm thick SiO$_2$ layer to form PS-*b*-(Py-Pt$_{1.0}$@P4VP) and (DT-Ag$_{1.0}$@PS)-*b*-P4VP layers. The subscripted number 1.0 is the prescribed total weight ratio between the Py-Pt (or DT-Ag) NPs and the P4VP (or PS) blocks. Thin films of the NP/block copolymer (DT-Ag$_{1.0}$@PS)-*b*-(Py-Pt$_{1.0}$@P4VP) were prepared by mixing Py-Pt NPs and PS-*b*-P4VP in pyridine, drying to form the PS-*b*-(Py-Pt@P4VP) composites, and then adding DT-Ag NPs to the PS-*b*-(Py-Pt@P4VP) in toluene to form the final films (detailed procedures for preparing the samples are provided in the

Experimental section). The wafers presenting the composite diblock copolymer/metal NP films were quickly transferred to a vacuum chamber for deposition of a 90 nm thick pentacene layer. Finally, a 40 nm thick Au film was thermally evaporated onto the pentacene film through a shadow mask to form the source and drain (S/D) electrodes.

Experimental

Nanoparticles

In the modified one-phase synthesis of the Py-Pt NPs, H$_2$PtCl$_6$ (50 mg mL^{-1}) and trioctylphosphine (TOP) were dissolved in EtOH at a molar ratio of 1 : 2 under vigorous stirring; the mixture was slowly added dropwise to an EtOH solution saturated with NaBH$_4$ and stirred further for 24 h. (Adding the precursor solution slowly to a saturated NaBH$_4$ solution resulted in a significantly lower polydispersity in particle size.) The precipitated product was isolated through centrifugation, dried under vacuum at room temperature, and then washed several times with toluene and EtOH to remove residual free ligands. The resulting TOP-protected Pt (TOP-Pt) NPs were dissolved in pyridine and heated at 65 °C for 6 h to obtain the final Py-Pt NPs, which were then precipitated out upon the addition of hexane.

In the modified one-phase synthesis of the dodecanethiol-passivated Ag NPs, AgNO$_3$ (15 mg mL^{-1}) and dodecanethiol were dissolved at a 1 : 1 molar ratio in anhydrous EtOH; the mixture was then added to an anhydrous EtOH solution saturated with NaBH$_4$ and stirred for 24 h. The product was precipitated and separated through centrifugation and then dried under vacuum at room temperature. To remove residual free thiols, the product was redissolved in hexane, precipitated upon the addition of EtOH, and then dried under vacuum.

Copolymer/NP composites

A pyridine solution containing 0.1 wt% PS$_{56k}$-*b*-P4VP$_{8k}$ (polydispersity index, 1.07) and Py-Pt NPs (of the same weight ratio as the P4VP block in the solution) was vigorously stirred and then dried under vacuum to provide the PS-*b*-(Py-Pt$_{1.0}$@P4VP) composites. This composite was redispersed in toluene by stirring vigorously for 2 days. Subsequently, two toluene solutions of neat PS-*b*-P4VP and PS-*b*-(Py-Pt$_{1.0}$@P4VP) composites were mixed with a toluene solution of the DT-Ag NPs, providing solutions containing a prescribed weight ratio of 1.0 for the total DT-Ag NPs and the PS blocks. On the other hand, a toluene solution of this composite was mixed at various ratios with a toluene solution of the DT-Ag NPs, providing solutions containing prescribed weight ratios (*c*) of the total DT-Ag NPs and the PS blocks of 0.4, 0.6, 0.8, 1.0, 1.2, and 1.4. These final mixtures were cast to obtain the composites, either on carbon-coated Cu grids for transmission electron microscopy (TEM) measurements or on Si wafer substrates (5000 rpm, 60 s) for atomic force microscopy (AFM) measurements and GISAXS measurements. All of the cast thin films were dried under vacuum at room temperature.

TEM and AFM imaging

TEM images were recorded using an FEI T12 transmission electron microscope with a low-energy electron beam (120 keV)
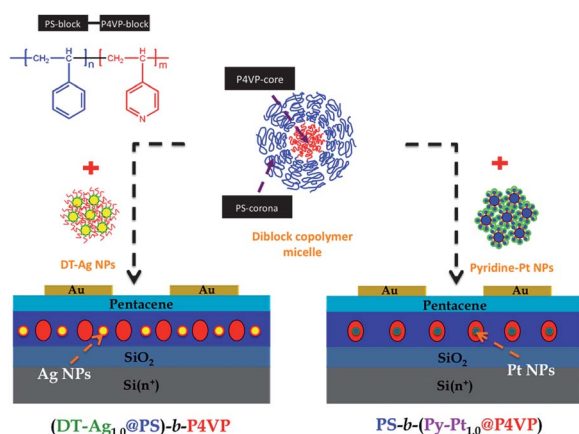

Fig. 1 Schematic representation of the device structures of pentacene-based OFET memory devices and the distributional positions of the DT-Ag and Py-Pt NPs within them. Inset: chemical structure of PS-*b*-P4VP copolymer.

This journal is © The Royal Society of Chemistry 2012

J. Mater. Chem., 2012, **22**, 454–461 | 455

to provide sufficient contrast to distinguish the PS and P4VP domains in all of the samples, without heavy ion staining. Cross-sectional TEM images of the fabricated OFET memory device based on a (DT-Ag$_{1.0}$@PS)-b-P4VP monolayer, the (DT-Ag$_{0.8}$@PS)-b-(Py-Pt$_{1.0}$@P4VP) monolayer, and the neat PS-b-P4VP films were recorded using an FEI Tecnai F-20 transmission electron microscope; samples were spin-cast onto Si (or Si–SiO$_2$) wafer substrates, then sectioned using an FEI Quanta 3D-FEG focused ion beam instrument. AFM images were obtained using a Digital Instruments Nanoscope III apparatus equipped with a NANOSENSORS silicon tip, operated in the tapping mode with a resonance frequency of 130 kHz.

GISAXS

Grazing-incidence small-angle X-ray scattering (GISAXS) measurements were conducted at the BL23A SWAXS endstation of the National Synchrotron Radiation Research Center in Taiwan. Two sets of instrument configurations—15 keV/2.4 m and 8 keV/5.0 m—were used for the X-ray beam energy and sample-to-detector distance, respectively, to cover a wide scattering range. GISAXS profiles were obtained from the corresponding GISAXS 2D images along the in-plane direction q_x, with q_z fixed at the specular beam position; q_x and q_z are the components of the scattering wavevector (defined by $4\pi\lambda^{-1}\sin\theta$, with the scattering angle 2θ) in the in-plane and out-of-plane directions, respectively.

Device fabrication

A heavily doped n-type silicon (n$^+$-Si) wafer and a 200 nm thick thermally oxidized SiO$_2$ film were used as the gate and dielectric of the OFET memory, respectively. The substrates were cut into 2 × 2 cm^2 pieces through mechanical scribing. Prior to deposition, the substrates were cleaned with acetone and isopropanol in an ultrasonic bath. The pure diblock copolymer and various polymer electrets, namely PS-b-P4VP, PS-b-(Py-Pt$_{1.0}$@P4VP), (DT-Ag$_{1.0}$@PS)-b-P4VP, and (DT-Ag$_{1.0}$@PS)-b-(Py-Pt$_{1.0}$@P4VP), were dissolved in toluene (forming 0.1 wt% solutions) and coated on a 200 nm thick SiO$_2$ layer (C_i = 17.275 nF cm^{-2}) via spin-coating (5000 rpm). The wafers were then quickly transferred to a vacuum chamber for deposition of the active layer. The semiconductor layer, 90 nm thick pentacene (Sigma-Aldrich; used without further purification), was then deposited at a growth rate of 0.2 Å s^{-1} and a base pressure of 6 × 10^{-6} torr. Finally, a 40 nm thick Au film was thermally evaporated onto the pentacene film through a shadow mask to form the S/D electrodes. The length and width of the channel were 250 and 2000 μm, respectively. The electrical characteristics of the devices were measured, using a Keithley 4200 semiconductor parameter analyzer, at room temperature under N$_2$ inside a glove box.

Results and discussion

Metal NPs of low polydispersity in terms of particle size are preferable when preparing organized NP/copolymer composite films. Using transmission electron microscopy (TEM; see Fig. S1, ESI†), we determined the mean sizes of the passivated DT-Ag and Py-Pt NPs obtained through modified one-phase syntheses[27–29] to be 3.9 and 1.5 nm (not including ligands),

respectively, each with an acceptable polydispersity (ca. 20%). Fig. 2 displays TEM images of the (DT-Ag$_{1.0}$@PS)-b-(Py-Pt$_{1.0}$@P4VP) composites that we prepared by placing a drop of each composite solution onto a Cu net and drying for 24 h prior to observation. The sequestration of the Pt and Ag NPs into the P4VP and PS blocks, respectively, of the highly asymmetric PS-b-P4VP monolayer micelles, was confirmed in the representative TEM images of the neat copolymer and the PS-b-(Py-Pt$_{1.0}$@P4VP), (DT-Ag$_{1.0}$@PS)-b-P4VP, and (DT-Ag$_{1.0}$@PS)-b-(Py-Pt$_{1.0}$@P4VP) composites. In Fig. 2a and b, the expanded size of the Py-Pt@P4VP cores (ca. 30 nm) relative to that of the neat P4VP (ca. 25 nm) is indicative of the successful incorporation of the Py-Pt NPs into the P4VP cores, resulting in enhanced TEM contrast between the PS and P4VP domains. Fig. 2c and d reveal that the DT-Ag NPs covered nearly the entire PS phase (matrix) of the copolymer micelles, and closely surrounded the pure P4VP and Py-Pt@P4VP cores in the respective images. Because of the rigidity of the composite thin films and, therefore, difficulties in sample preparation, we could not obtain top-view TEM images of the films. Instead, we used grazing-incidence small-angle X-ray scattering (GISAXS) to probe the global structures of the films.

Grazing-incidence small-angle X-ray scattering (GISAXS) revealed further structural characteristics of the NP/copolymer micelle films cast on Si wafers. Fig. 3a displays a representative two-strip-like pattern observed for the composite film of (DT-Ag$_{0.8}$@PS)-b-(Py-Pt$_{1.0}$@P4VP), revealing in-plane-ordered monolayer micelles;[30,31] the corresponding in-plane GISAXS profile (Fig. 3c) features peaks that are consistent with those expected for two-dimensional (2D) hexagonal packing (i.e., a peak position ratio of 1 : 3$^{1/2}$: 2 for the first three peaks).[32] We estimated the mean spacing [$D = (4/3)^{1/2}d_{100}$] of the micelles from the first peak position[32] [at a value of the in-plane wave-vector transfer of X-rays (q_x) of 0.00329 Å^{-1}] to be 220 nm; this value is significantly larger than that (159 nm) similarly deduced for the neat copolymer from Fig. 3b and c, due to sequestration of the NPs. Moreover, the GISAXS pattern recorded in the higher-q_x
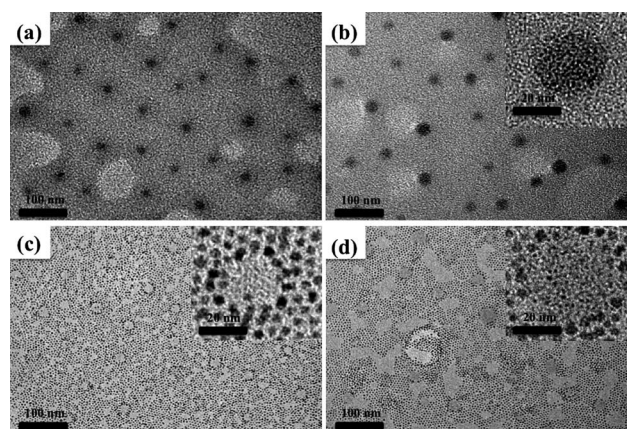

Fig. 2 TEM images of (a) PS-b-P4VP, (b) PS-b-(Py-Pt$_{1.0}$@P4VP), (c) (DT-Ag$_{1.0}$@PS)-b-P4VP, and (d) (DT-Ag$_{1.0}$@PS)-b-(Py-Pt$_{1.0}$@P4VP) composite films. The dark spots in (a) and (b) and the light spots in (c) and (d) represent P4VP cores, without or with the Py-Pt NPs. The dark spots in (c) and (d) represent the DT-Ag NPs. Insets: detailed view of single P4VP cores and their surroundings.
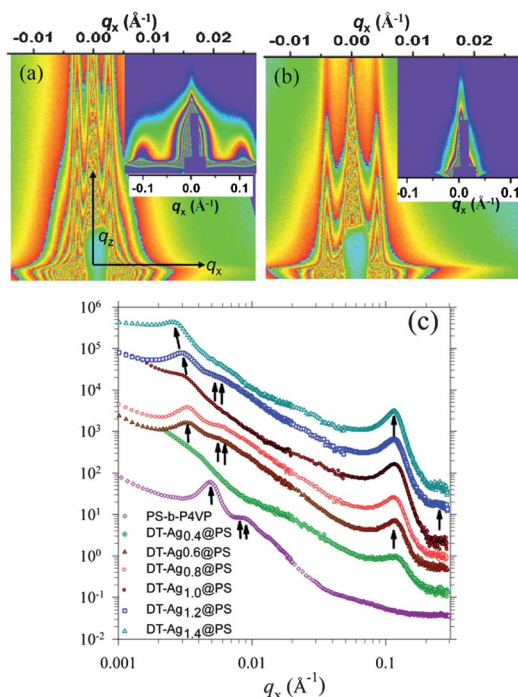
Fig. 3 Selected GISAXS patterns of (a) the (DT-Ag$_{0.8}$@PS)-b-(Py-Pt$_{1.0}$@P4VP) composite and (b) the neat PS-b-P4VP copolymer film. Insets: corresponding GISAXS patterns measured in a higher-q_x region. The peaks at 0.115 Å^{-1} arose from the short-range-ordered DT-Ag NPs. (c) In-plane GISAXS profiles for the neat copolymer and composites incorporating Py-Pt NPs and DT-Ag NPs, with concentrations of the latter (c) of 0.4, 0.6, 0.8, 1.0, 1.2, and 1.4. The arrows indicate selective scattering peaks from the hexagonally ordered copolymer micelle cores in the lower-q_x region and the short-range-ordered DT-Ag NPs in the higher-q_x region, respectively.

region for the composite film revealed additional in-plane-ordering strips (at $q_x = 0.115$ Å^{-1}; inset of Fig. 3a), indicating that the DT-Ag NPs in the PS phase were also in-plane-ordered over a much smaller length scale;[30] the corresponding mean spacing (5.5 nm), deduced from the peak position, is consistent with that observed in the TEM image in Fig. 2d (note that the ordering of the micelles is relatively weak in this TEM image with an oversaturated Ag NP loading (c) of 1.0, consistent with the less-pronounced low-q_x peaks in the GISAXS profile in Fig. 3c).

The series of DT-Ag concentration-dependent GISAXS profiles in Fig. 3c reveal the correlated hierarchical arrangement of Pt and Ag NPs in the monolayer of hexagonally ordered micelles. At a DT-Ag weight ratio (c) of 0.4 in the system, the first hexagonal ordering peak at 0.0045 Å^{-1} of the neat copolymer micelles was seriously dampened, presumably because of the distorted PS shells of the unevenly distributed DT-Ag NPs (detailed below). When the value of c increased to 0.6, the DT-Ag NPs underwent improved short-range ordering in the PS phase, as revealed by the sharpened peak at a value of q_x of 0.115 Å^{-1}; concomitantly, the intensity of the scattering peaks corresponding to the hexagonal packing of the micelle cores increased significantly, with the first peak shifting to a lower value of q_x (ca. 0.0033 Å^{-1}); the corresponding micelle spacing (D) expanded to 220 nm. Further increasing the DT-Ag concentration (c) to 0.8 resulted in concomitant enhancements in the short-range

ordering peak of the DT-Ag NPs in the PS phase and the hexagonal ordering peaks of the Py-Pt/P4VP micelle cores. The D-spacing (or scattering peak positions), however, changed only marginally, implying that the added DT-Ag NPs were all accommodated in the PS phase (without significantly stretching the PS chain conformation) to provide more homogeneous complex blocks. When the weight ratios (c) were 1.0, 1.2, and 1.4, the added DT-Ag NPs expanded the mean micelle spacing to 234, 241, and 286 nm, respectively (Fig. 3c); we attribute the expanding of the D-spacing in this stage to PS chain stretching forced by the oversaturated DT-Ag NPs. Consequently, the scattering peaks of the hexagonal packing of the Py-Pt/P4VP cores deteriorated slightly. From these results, an optimized loading of the DT-Ag NPs (ca. 0.8) in the PS blocks under a Py-Pt NP loading of 1.0 within the P4VP blocks provided relatively homogeneous complex blocks, which we expected to form a better 2D hierarchical arrangement of Pt and Ag NPs in the copolymer micelle film.

Fig. 4 displays selective AFM images for samples similar to those used in the GISAXS measurements. These images reveal consistent structural characteristics (hexagonal packing) and the effects of the DT-Ag NP concentration on the disordering ($c = 0.4$; Fig. 4b) and ordering ($c = 0.6$; Fig. 4c) of the Py-Pt@P4VP cores of the diblock copolymer micelle films. The mean micelle
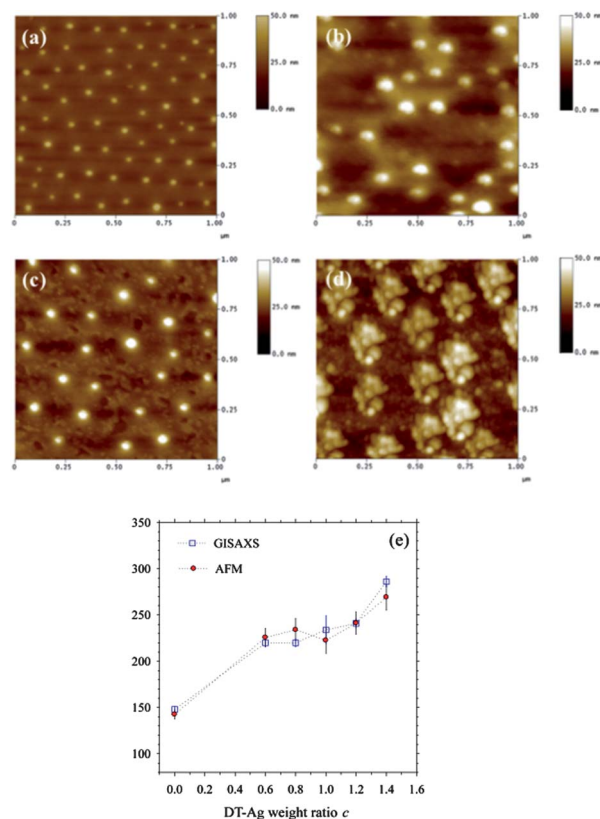

Fig. 4 Representative AFM patterns of the (a) neat PS-b-P4VP copolymer and (b–d) (DT-Ag$_c$@PS)-b-(Py-Pt$_{1.0}$@P4VP) composites [DT-Ag NP weight ratios (c): (b) 0.4, (c) 0.6, and (d) 1.2] on Si wafers. Bright spots (local high lands) represent P4VP or Py-Pt@P4VP cores. (e) Average core spacings, determined from the AFM images and GISAXS data, of various composites.

This journal is © The Royal Society of Chemistry 2012

J. Mater. Chem., 2012, **22**, 454–461 | 457

spacings estimated from the AFM images are consistent with those observed using GISAXS (Fig. 4e). The larger and smeared bright spots in Fig. 4d for the composite film at a value of c of 1.2 may have resulted from oversaturated DT-Ag NPs accumulating around the P4VP cores. Similarly, at low concentrations of DT-Ag NPs, we observed (TEM) that these small DT-Ag NPs (4 nm) preferred to reside in the large PS matrix phase (>200 nm) at the interfaces between the PS and P4VP blocks, before reaching the optimal NP loading for a homogeneous hybrid film. The preferred positioning of the small DT-Ag NPs at the interfaces of the two dissimilar blocks in the large PS matrix phase is consistent with theoretical predictions.[33,34] All these correlated and consistent morphological changes observed using GISAXS and AFM indicate that the DT-Ag NPs interacted collectively with the copolymer (through their incorporation and organization in the PS phase) and enhanced the ordering of the global structure of the NP/copolymer film. Had the DT-Ag NPs segregated from the copolymer, we would not have observed the correlated hierarchical ordering of the DT-Ag NPs (locally) and the block copolymer micelles (globally), as a function of DT-Ag NP loading concentration.

Fig. 5a–e display plots of the drain–source current (I_{DS}) *versus* the drain–source voltage (V_{DS}) for OFETs with various composite electrets, with gate voltages (V_g) ranging from 0 to -10 V at the step of -2 V. The OFET parameters for these samples—the field-effect mobilities, the on/off ratio (I_{on}/I_{off}), and the threshold voltages (V_t)—were obtained using eqn (1):[35]

$$I_{ds} = \frac{1}{2}\frac{W}{L}\mu_{FET}C_i(V_g - V_t)^2 \tag{1}$$

where I_{ds} is the source–drain current, W is the width of the channel, L is the length of the channel, μ_{FET} is the field-effect mobility, C_i is the capacitance per unit area of the gate insulator, V_g is the gate voltage, and V_t is the threshold voltage. Fig. 5f summarizes the mobilities and threshold voltages for bare SiO_2, PS-*b*-P4VP, PS-*b*-(Py-Pt$_{1.0}$@P4VP), (DT-Ag$_{1.0}$@PS)-*b*-P4VP, and (DT-Ag$_{1.0}$@PS)-*b*-(Py-Pt$_{1.0}$@P4VP) that were determined using eqn (1). The calculated values of V_t for bare SiO_2, PS-*b*-P4VP, PS-*b*-(Py-Pt$_{1.0}$@P4VP), (DT-Ag$_{1.0}$@PS)-*b*-P4VP, and (DT-Ag$_{1.0}$@PS)-*b*-(Py-Pt$_{1.0}$@P4VP) were -4.8, -1.1, -2.6, -1.8, and -2.5 V, respectively; the I_{on}/I_{off} ratios for these samples were on the order of 10^5. Although the field-effect mobilities of the devices incorporating (DT-Ag$_{1.0}$@PS)-*b*-P4VP and (DT-Ag$_{1.0}$@PS)-*b*-(Py-Pt$_{1.0}$@P4VP) were slightly lower than those of the bare SiO_2, PS-*b*-P4VP, and PS-*b*-(Py-Pt$_{1.0}$@P4VP), these samples still functioned as p-channel OFETs, suggesting that the addition of different composite layers did not degrade the performance of the devices.

Fig. 6a presents a cross-sectional TEM image of the fabricated OFET memory device incorporating a layer of the (DT-Ag$_{1.0}$@PS)-*b*-P4VP composite; the DT-Ag NPs were located directly above the Si–SiO_2 substrate, embedded in the micelle monolayer, rather than being located merely on the surface of the PS phase. If these DT-Ag NPs were located on the surface of the PS phase, then a portion of them would also have been located on the Si–SiO_2 substrate, with the rest located close to the top surface, along with a vertical distribution to the substrate plane. The short-range ordering of the DT-Ag NPs appears blurred in Fig. 6b because of the overlapped NPs in the side-projected view, relative to the clearer top view in Fig. 2c. Furthermore, Fig. S2† displays cross-sectional TEM images of monolayers (film thickness: *ca.* 30 nm) of the (DT-Ag$_{0.8}$@PS)-*b*-(Py-Pt$_{1.0}$@P4VP) composite and the neat copolymer; energy-dispersive X-ray (EDX) spectra (see Fig. S3, ESI†) confirmed that the Pt and Ag NPs were located in the P4VP cores and in the PS matrix, respectively, of the copolymer.

Fig. 7a–e reveal the V_t shifts in the transfer curves of the OFETs incorporating the various composites. These devices were subject to a programmed gate bias of 60 V and an erasing gate bias of -60 V within the time of 3 s. No positive V_t shift is apparent in Fig. 7a, indicating that the OFET employing the bare SiO_2 layer did not trap any positive or negative charge in the gate insulator. When neat PS-*b*-P4VP was inserted between the
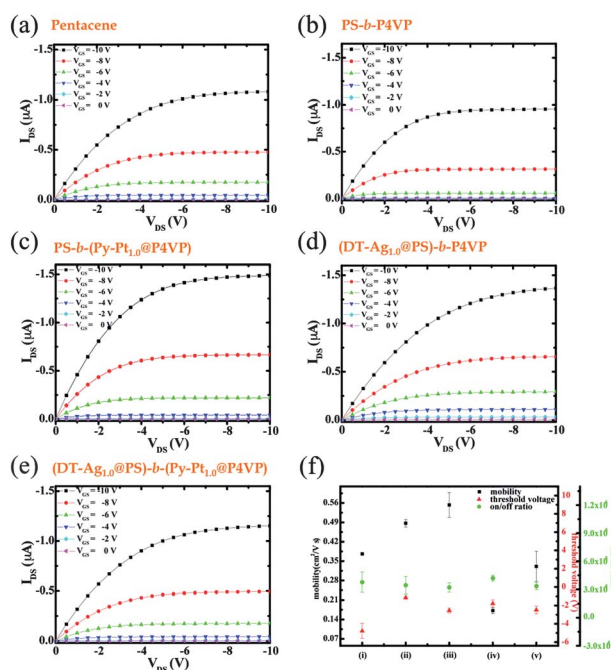

Fig. 5 Output characteristics of OFET memory devices incorporating (a) bare SiO_2, (b) PS-*b*-P4VP, (c) PS-*b*-(Py-Pt$_{1.0}$@P4VP), (d) (DT-Ag$_{1.0}$@PS)-*b*-P4VP, and (e) (DT-Ag$_{1.0}$@PS)-*b*-(Py-Pt$_{1.0}$@P4VP). (f) Plots of the mobilities (■), threshold voltages (▲), and on/off ratios (●), with error bars, for the devices in (a–e).
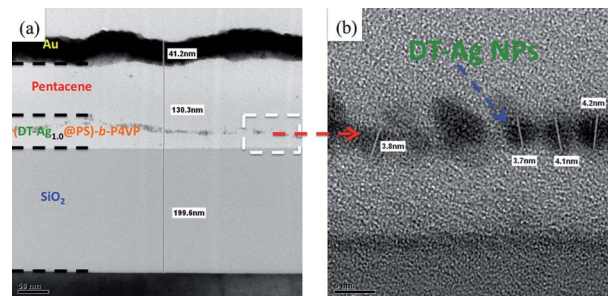

Fig. 6 (a) Cross-sectional TEM image of the fabricated OFET memory device based on a monolayer of the (DT-Ag$_{1.0}$@PS)-P4VP micelles. (b) Detailed view of the square zone marked in (a). The gray spheres having an average diameter of *ca.* 4 nm are the Ag NPs.

pentacene and SiO_2 layer, the OFET threshold voltage shifted to the positive regime, with a value of V_t of approximately 21.8 V. We speculate that the memory effect of the pristine asymmetric PS_{56k}-b-$P4VP_{8k}$ block copolymer thin film was due to electron trapping by the P4VP spheres in the PS matrix. When 100 wt% of the high-work-function Py-Pt metal NPs was present in the P4VP block [$i.e.$, for PS-b-(Py-$Pt_{1.0}$@P4VP)], additional electron trapping by these metal NPs further enhanced the memory window to 26.4 V, an increase of 21%. In contrast, the OFET threshold voltage shifted toward the negative regime when 100 wt% of the low-work-function DT-Ag NPs was sequestered into the PS block [$i.e.$, for (DT-$Ag_{1.0}$@PS)-b-P4VP]; the device exhibited a negative V_t shift, with a value of 18.6 V, as a result of hole trapping by the Ag NPs in the PS block. Therefore, the positive or negative V_t shifts in these types of OFET memory devices are determined by a combination of the type of diblock copolymer and, more critically, the type of metal NPs. When 100 wt% of the high-work-function Py-Pt metal NPs and 100 wt% of the low-work-function DT-Ag NPs were present in the P4VP and PS blocks, respectively [$i.e.$, for (DT-$Ag_{1.0}$@PS)-b-(Py-$Pt_{1.0}$@P4VP)], the memory window decreased to a negative V_t shift, with a value of 11.3 V, due to the large difference in the volume fractions of the PS and P4VP blocks and, therefore, the amounts of Ag and Pt NPs, resulting in a comprised effect caused by the hole trapping ability of the DT-Ag NPs and the electron trapping ability of the Py-Pt NPs. Fig. 7f presents the energy level diagram of the OFET. The electric field accelerated electrons in the pentacene units near the interface to tunnel into the PS layer, where they were trapped by the Pt NPs. Because of the existence

of a large potential barrier between the Pt NPs and the lowest unoccupied molecular orbital (LUMO) of the PS layer, the electrons were confined to a potential well and charge could be stored in the Pt NPs. Therefore, when the device was subjected to appropriate programming and erasing gate voltage, we could measure a memory window of greater than 20 V and an onset voltage. When we incorporated Ag NPs, lower-work-function metal NPs, in place of Pt NPs, although the electric field could induce the electrons to tunnel through the PS layer and into the Ag NPs, the electrons were not confined by the smaller potential well and we did not observe a positive V_t shift. In contrast, when the device was subjected to a negative applied electric field, the holes were confined by the potential barrier between the work function of the Ag NPs and highest occupied molecular orbital (HOMO) of the PS layer. As a result, we observed a negative V_t shift of the transfer curve. To further enhance the memory window, the insulator layer thickness could be attenuated[7] or the active layer thickness could be optimized.

Table 1 lists the measured values of the typical field-effect mobility (μ_{FET}), the initial V_t, and I_{on}/I_{off} determined from the conventional characterization equation (eqn (1)). We calculated the amount of transferred charge (Δn) from the shift in V_t after the programming process[36] according to:

$$\Delta n = \frac{\Delta V_t C_i}{e} \qquad (2)$$

where e, ΔV_t, and C_i are the element charge, the shift in V_t, and the capacitance of the gate dielectric, respectively. According to eqn (2), the amount of transferred charge was proportional to the threshold voltage shift and the capacitance of the gate dielectric. The amount of transferred charge indicated that carriers were trapped in the metal NPs. Table 1 indicates the largest amount of transferred charge (the capacitance) and the threshold voltage shift was that in the device incorporating PS-b-(Py-$Pt_{1.0}$@P4VP), more than that of the device incorporating (DT-$Ag_{1.0}$@PS)-b-P4VP. In theory, the amount of transferred charges is proportional to the amount of sequestered metal NPs.

This situation may result from the device incorporating PS-b-(Py-$Pt_{1.0}$@P4VP) exhibiting the largest energy barrier between the LUMO of PS and the work function of Pt, making it difficult for the carriers to escape from this potential well merely by thermal energy at room temperature. In addition, the probability of electrons tunneling through the PS layer is larger than that for holes,[32] meaning that more electrons could be trapped in the Pt NPs. To further improve the amount of transferred charge, the device should incorporate a larger concentration of NPs, a thinner gate dielectric, and suitable metal NPs to ensure a larger energy barrier between the work functions of the metal NPs and the tunnel oxide layer.

For the non-volatile memory applications, the measurements of the program/erase speed and the retention time of our device were carried out. Fig. 8a and b present the reversible switching behavior of a pentacene OFET memory utilizing PS_{56k}-b-$P4VP_{8k}$ that incorporates Pt nanoparticles, PS-b-(Py-$Pt_{1.0}$@P4VP), in a series of programming ($V_g = 60$ V, $V_d = -10$ V) and erasing ($V_g = -60$ V, $V_d = -10$ V) processes. The retention time of the shifted characteristics after programming and erasing operations is presented in Fig. 8c; the curves in Fig. 8c indicate that the retention time is more than 10^6 s, which is our experiment
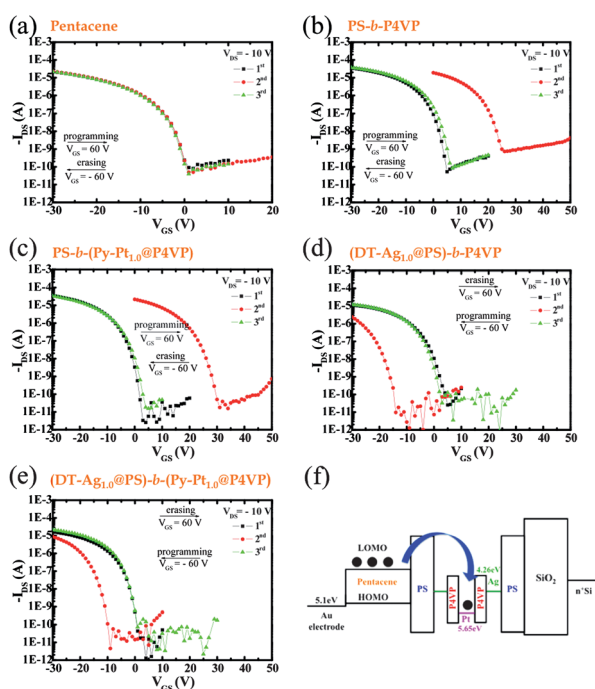

Fig. 7 Threshold voltage shifts in the transfer curves of the devices incorporating (a) bare SiO_2, (b) PS-b-P4VP, (c) PS-b-(Py-$Pt_{1.0}$@P4VP), (d) (DT-$Ag_{1.0}$@PS)-b-P4VP, and (e) (DT-$Ag_{1.0}$@PS)-b-(Py-$Pt_{1.0}$@P4VP). (f) Schematic representation of the carrier tunneling through the polymer electret into the metal NPs.

This journal is © The Royal Society of Chemistry 2012

J. Mater. Chem., 2012, **22**, 454–461 | 459

Table 1 Measured fundamental OFET-type memory characteristics: field-effect mobility (μ_{FET}), on/off ratio (I_{on}/I_{off}), threshold voltage (V_t), V_t shift, and the amount of transferred charge (Δn)

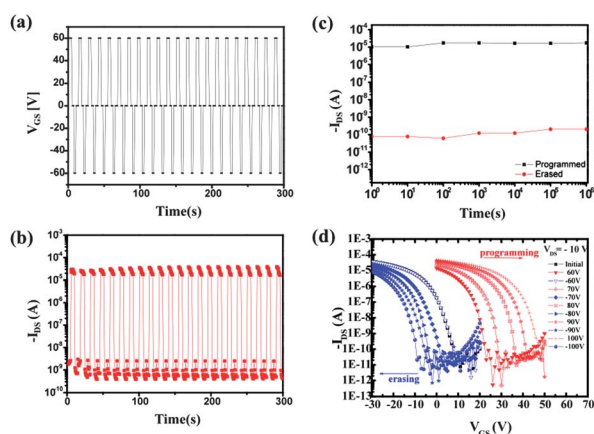|	μ_{FET}/cm² V⁻¹ S⁻¹	I_{on}/I_{off}	Initial V_t/V	V_t shifts/V	Δn
Positive V_t shifts					
Bare SiO₂	0.38 ± 0.01	10⁵	−4.8 ± 0.8	Negligible	Negligible
PS-*b*-P4VP	0.49 ± 0.02	10⁵	−1.1 ± 0.1	21.8 ± 0.2	2.4 × 10¹²
PS-*b*-(Py-Pt$_{1.0}$@P4VP)	0.55 ± 0.05	10⁵	−2.6 ± 0.3	26.4 ± 1.1	2.9 × 10¹²
Negative V_t shifts					
(DT-Ag$_{1.0}$@PS)-*b*-P4VP	0.17 ± 0.01	10⁵	−1.8 ± 0.4	18.6 ± 0.7	2.0 × 10¹²
(DT-Ag$_{1.0}$@PS)-*b*-(Py-Pt$_{1.0}$@P4VP)	0.33 ± 0.05	10⁵	−2.5 ± 0.4	11.3 ± 1.2	1.2 × 10¹²

Fig. 8 (a) Program/erase bias pulses of ±60 V were repeatedly applied to the bottom-gate electrode for 5 s (programming: $V_g = 60$ V and $V_d = -10$ V and erasing: $V_g = -60$ V and $V_d = -10$ V). (b) Reversible switching of a pentacene OFET memory utilizing PS-*b*-(Py-Pt$_{1.0}$@P4VP) for on- and off-current states. (c) The retention time for the PS-*b*-(Py-Pt$_{1.0}$@P4VP) memory devices in the programmed/erased states under ambient conditions at room temperature. The dotted line is an extrapolation of the measured data for the retention capability to determine the long-term reliability of the memory devices. (d) Shifts in transfer curves at $V_d = -10$ V for the OFET memory device, where $V_g = 60, 70, 80, 90,$ 100 V and $V_g = -60, -70, -80, -90, -100$ V were applied for 3 s for programming and erasing, respectively.

duration, with the on/off ratio maintained at 10⁵. At the same time, the effects of different programmed/erased voltages on the PS-*b*-P4VP memory cell are displayed in Fig. 8d, which shows the memory window increases with the programmed voltages, indicating its good potential for applications.

Conclusions

We have demonstrated that p-channel-type non-volatile OFET memory devices can be fabricated using an asymmetric PS-*b*-P4VP layer that incorporates metal NPs of different work functions specifically in various blocks. The transfer curves of non-volatile OFET memory devices incorporating an asymmetric PS$_{56k}$-*b*-P4VP$_{8k}$ layer embedded with high-work-function Pt NPs in the P4VP block exhibited a positive threshold voltage shift and a large memory window (*ca.* 27 V). On the other hand, the transfer curves of non-volatile OFET memory devices incorporating an asymmetric PS$_{56k}$-*b*-P4VP$_{8k}$ layer embedded with low-work-function Ag NPs exhibited a negative threshold voltage shift and a memory window of *ca.* 19 V.

Note added after first publication

This article replaces the version published on 9th November 2011, which contained an error in the PDF version. There was an error in equation 1 which has now been corrected.

References

1 J. Quyang, C. W. Chu, C. R. Szmanda, L. Ma and Y. Yang, *Nat. Mater.*, 2004, **3**, 918.
2 Q. D. Ling, Y. Song, S. J. Ding, C. X. Zhu, D. S. H. Chan, D. L. Kwong, E. T. Kang and K. G. Neoh, *Adv. Mater.*, 2005, **17**, 455.
3 C. W. Chu, J. Quyang, J. H. Tseng and Y. Yang, *Adv. Mater.*, 2005, **17**, 1440.
4 D. Wei, J. K. Baral, R. Osterbacka and A. Ivaska, *J. Mater. Chem.*, 2008, **18**, 1853.
5 W. L. Leong, P. S. Lee, A. Lohani, Y. M. Lam, T. Chen, S. Zhang, A. Dodabalapur and S. G. Mhaisalkar, *Adv. Mater.*, 2008, **20**, 2325.
6 J. S. Lee, Y. M. Kim, J. H. Kwon, H. Shin, B. H. Sohn and J. Lee, *Adv. Mater.*, 2009, **21**, 178.
7 C. C. Chen, M. Y. Chiu, J. T. Shun and K. H. Wei, *Appl. Phys. Lett.*, 2008, **92**, 143105.
8 K. J. Baeg, Y. Y. Noh, J. Ghim, S. J. Kang, H. Lee and D. Y. Kim, *Adv. Mater.*, 2006, **18**, 3179.
9 K. J. Baeg, Y. Y. Noh, J. Ghim, B. Lim and D. Y. Kim, *Adv. Funct. Mater.*, 2008, **18**, 3678.
10 P. C. Wu, Y. Dai, Y. Ye, X. L. Fang, T. Sun, C. Liu and L. Dai, *J. Mater. Chem.*, 2010, **20**, 4404.
11 K. J. Baeg, Y. Y. Noh, H. Sirringhaus and D. Y. Kim, *Adv. Funct. Mater.*, 2010, **20**, 224.
12 Y. Guo, G. Yu and Y. Liu, *Adv. Mater.*, 2010, **22**, 4427.
13 Q. D. Ling, D. J. Liaw, C. Zhu, D. S. H. Chan, E. T. Kang and K. Neoh, *Prog. Polym. Sci.*, 2008, **33**, 917.
14 C. W. Tseng and Y. T. Tao, *J. Am. Chem. Soc.*, 2009, **131**, 12441.
15 M. Y. Chiu, C. C. Chen, J. T. Sheu and K. H. Wei, *Org. Electron.*, 2009, **10**, 769.
16 J. He, R. Tangirala, T. Emrick, T. P. Russell, A. Boker, X. Li and J. Wang, *Adv. Mater.*, 2007, **19**, 381.
17 Q. Li, J. He, E. Glogowski, X. Li, J. Wang, T. Emrick and T. P. Russell, *Adv. Mater.*, 2008, **20**, 1462.
18 J. P. Spatz, S. Sheiko and M. Moller, *Macromolecules*, 1996, **29**, 3220.
19 J. P. Spatz, A. Roescher and M. Moller, *Adv. Mater.*, 1996, **8**, 337.
20 N. Sakamoto, M. Harada and T. Hashimoto, *Macromolecules*, 2006, **39**, 1116.
21 C. Mendoza, N. Gindy, J. S. Gutmann, A. Fromsdorf, S. Forster and A. Fahmi, *Langmuir*, 2009, **25**, 9571.
22 W. L. Leong, N. Mathews, S. Mhaisalkar, Y. M. Lam, T. Chen and P. S. Lee, *J. Mater. Chem.*, 2009, **19**, 7354.
23 M. R. Bockstaller, Y. Lapetnikov, S. Margel and E. L. Thomas, *J. Am. Chem. Soc.*, 2003, **125**, 5276.

24 J. J. Chiu, B. J. Kim, E. J. Kramer and D. J. Pine, *J. Am. Chem. Soc.*, 2005, **127**, 5036.

25 C. P. Li, K. H. Wei and J. Y. Huang, *Angew. Chem., Int. Ed.*, 2006, **45**, 1449.

26 C. M. Huang, K. H. Wei, U. S. Jeng and H. S. Sheu, *Macromolecules*, 2008, **41**, 6876.

27 S. Y. Kang and K. Kim, *Langmuir*, 1998, **14**, 226.

28 T. Teranishi, I. Kiyokawa and M. Miyaka, *Adv. Mater.*, 1998, **10**, 596.

29 M. Brust, M. Walker, D. Bethell, D. J. Schiffrin and R. Whyman, *J. Chem. Soc., Chem. Commun.*, 1994, 801.

30 G. Renaud, R. Lazzari and F. P. Leroy, *Surf. Sci. Rep.*, 2009, **64**, 255.

31 S. Park, J.-Y. Wang, B. Kim, J. Xu and T. P. Russell, *ACS Nano*, 2008, **2**, 766.

32 S.-W. Yeh, K.-H. Wei, Y.-S. Sun, U. Jeng and K. S. Liang, *Macromolecules*, 2003, **36**, 7903.

33 M. R. Thompson, V. V. Ginzburg, M. W. Matsen and A. C. Balazs, *Science*, 2001, **292**, 2469.

34 J. Y. Lee, R. B. Thompson, D. Jasnow and A. C. Balazs, *Macromolecules*, 2002, **35**, 4855.

35 A. D. Neamen, in *Semiconductor Physics and Devices: Basic Principles*, McGraw-Hill, Dubuque, 2003.

36 V. Podzorov and M. E. Gershenson, *Phys. Rev. Lett.*, 2005, **95**, 016602.